Advances in Nano Research, *Vol. 18, No. 5 (2025) 489-502*
https://doi.org/10.12989/anr.2025.18.5.489

Improving concrete properties through nano-modification: Advances in mechanical strength, durability, and structural performance

Chunhua Huang[1,2], Shichao He*[1,2], Zixun Xiong[3] and Belgacem Bouallegue[4]

[1]*School of Intelligent Construction, Luzhou vocational and technical college, Luzhou 646000, China*
[2]*Luzhou Key Laboratory of Intelligent Construction and Low-carbon Technology, Luzhou 646000, Sichuan, China*
[3]*Luzhou Xuxing Concrete Co., Ltd, Luzhou 646000, Sichuan, China*
[4]*Department of Computer Engineering, College of Computer Science, King Khalid University, ABHA, 61421, Saudi Arabia*

(*Received February 7, 2025, Revised April 8, 2025, Accepted April 8, 2025*)

Abstract. This study investigates the enhancement of structural and dynamic performance in concrete materials through nano-modification using nano-alumina reinforcements. Emphasis is placed on curved concrete shell panels, where geometric complexity and material heterogeneity present challenges in mechanical stability and vibrational behavior. Nano-alumina particles are introduced in varying distribution patterns (Pattern A to Pattern X) to improve stiffness, mechanical strength, and overall durability. Through a detailed parametric analysis, the influence of foundation stiffness—represented by the dimensionless Winkler and Pasternak parameters on the relative frequency change (RFC) is evaluated. The study also assesses the impact of geometric ratios such as thickness-to-length and radius-to-length on natural frequencies. Results reveal that increasing nano-alumina content and optimizing its distribution lead to significant improvements in natural frequency response and relative frequency stability under various boundary and loading conditions. Comparative analysis with classical and higher-order shear deformation theories further validates the proposed model, demonstrating close agreement with Reddy's third-order shear predictions. These findings highlight the effectiveness of nano-modification in improving the dynamic behavior of concrete structures, suggesting promising applications in advanced construction materials and structural systems where vibration control and mechanical resilience are critical.

Keywords: curved concrete shell panels; nano-alumina reinforced concrete; nanocomposite structural enhancement; Pasternak and Winkler foundation models; relative frequency change

1. Introduction

Nanocomposite reinforcement has emerged as a transformative advancement in engineering materials due to its exceptional mechanical, thermal, and functional properties (Azmi *et al.* 2019). By integrating nanomaterials such as graphene, carbon nanotubes, or nanoclays into traditional matrices, engineers can achieve superior strength-to-weight ratios and enhanced durability (Ebrahimi *et al.* 2019a). These materials exhibit remarkable stiffness and strength at low filler concentrations, allowing for lightweight structural designs without compromising performance (Ebrahimi *et al.* 2019b). Nanocomposites also offer improved resistance to fatigue, fracture, and environmental degradation, making them ideal for high-performance applications (Hajmohammad *et al.* 2018). In thermal management, their superior conductivity enables efficient heat dissipation in electronic and aerospace components (Jayakumari *et al.* 2024). Their multifunctional capabilities further allow for the integration of self-sensing, self-healing, and energy-harvesting functions within structural systems (Madenci *et al.* 2023). For civil and mechanical engineers, nanocomposite-reinforced structures promise longer service life and reduced maintenance costs (Moradi *et al.* 2022). In the biomedical field, tailored nanocomposites enable the development of biocompatible implants with improved mechanical compatibility (Xia *et al.* 2023). Furthermore, advances in computational modeling and experimental techniques facilitate the precise design and optimization of nanocomposite architectures (Ye *et al.* 2024). Overall, nanocomposite reinforcement is revolutionizing material engineering by enabling the development of smarter, stronger, and more sustainable systems (Zerrouki *et al.* 2020).

Stability analysis is a fundamental aspect of structural engineering, ensuring that structures can withstand applied loads without experiencing sudden or catastrophic failure (Zhao *et al.* 2022). It enables engineers to predict critical conditions under which structures may buckle, collapse, or lose equilibrium (Liu *et al.* 2021a). Accurate stability assessment is essential for designing safe and reliable buildings, bridges, aerospace components, and mechanical systems (Bentrar *et al.* 2023, Beitollahi *et al.* 2025). Through stability analysis, engineers can identify load-bearing limitations and optimize material usage while maintaining structural integrity (Gawah *et al.* 2025). It plays a vital role in evaluating the effects of geometric imperfections, residual stresses, and nonlinear behaviors on structural performance (Gawah *et al.* 2024). In advanced systems, such as slender or composite structures, stability considerations become even more critical due to their

*Corresponding author, Ph.D.,
E-mail: 393763536@qq.com

ISSN: 2287-237X (Print), 2287-2388 (Online)

sensitivity to loading and environmental conditions (Youzera *et al*. 2025). The integration of analytical, numerical, and experimental methods enhances the precision of stability predictions under various boundary and loading conditions (Al-Houri *et al*. 2024). Moreover, stability analysis informs maintenance strategies and retrofitting decisions for aging infrastructure (Tounsi *et al*. 2024). For innovative designs involving smart materials or nanostructured composites, stability analysis guides the safe application of emerging technologies (Belabed *et al*. 2024a). Ultimately, it serves as a cornerstone for sustainable, efficient, and resilient engineering solutions across multiple disciplines (Belabed *et al*. 2024b).

Machine learning (ML) algorithms have become powerful predictive tools in engineering, enabling data-driven insights and decision-making in complex systems (Samaniego *et al*. 2020). They allow engineers to model nonlinear relationships and uncover hidden patterns from large datasets that traditional methods may not capture effectively (Zhuang *et al*. 2021). By training on historical or simulated data, ML algorithms can predict structural behavior, material properties, system failures, and performance trends with high accuracy (Guo *et al*. 2021). These predictive capabilities significantly enhance the efficiency of design, monitoring, and control processes across various engineering domains (Eshaghi *et al*. 2025). ML techniques such as support vector machines, neural networks, and ensemble models are particularly useful for optimizing design parameters and forecasting system responses under uncertainty (Mortazavi *et al*. 2023). In civil, mechanical, and aerospace engineering, ML assists in damage detection, load prediction, and lifecycle assessment (He *et al*. 2022). For materials science, ML accelerates the discovery and optimization of advanced materials, including nanocomposites (Goswami *et al*. 2020). The integration of ML with simulation tools and sensor data enables real-time prediction and adaptive control in smart structures (Buaria and Sreenivasan 2023). Moreover, ML supports the development of digital twins, providing engineers with virtual models that evolve with real-time input for improved diagnostics and performance evaluation (Li *et al*. 2023). As engineering challenges grow in complexity, ML-based prediction stands as a critical component of intelligent and resilient system design (Wu *et al*. 2024).

Modeling plays a critical role in modern engineering (Li *et al*. 2024, Liu *et al*. 2024). It allows engineers to represent complex systems in a simplified, manageable way (Wang *et al*. 2025, Zhang *et al*. 2025). Through modeling, abstract ideas can be visualized, analyzed, and communicated effectively (Sun *et al*. 2017, Niu *et al*. 2024). This process helps engineers predict how systems will behave under various conditions. It also aids in identifying potential design flaws early in development (Long *et al*. 2024, Zhang *et al*. 2024). By using models, engineers save time and reduce costs associated with physical prototyping (Zhang *et al*. 2022, Rong *et al*. 2025). Computer-aided modeling enables simulations that mimic real-world scenarios with impressive accuracy (Huang *et al*. 2022, Khorshidi *et al*. 2022). These simulations provide valuable data without the need for extensive field testing (Chen *et al*. 2023, Yang *et al*. 2023a). Modeling supports innovation by allowing rapid iteration of design concepts (Song *et al*. 2024, Yang *et al*. 2024a). It also enhances decision-making by presenting data-driven insights (Yang *et al*. 2023b, 2024b). Whether in mechanical, civil, electrical, or software engineering, models are foundational tools (Hu *et al*. 2023, Wu *et al*. 2023). They facilitate collaboration among multi-disciplinary teams through a shared understanding (Han *et al*. 2023a, b). Models also serve as documentation that guides future development and maintenance (Liu *et al*. 2021b, Taheri *et al*. 2021). In safety-critical fields like aerospace or biomedical engineering, modeling is essential for risk assessment (Taheri *et al*. 2020, Feng *et al*. 2021). It helps ensure that systems meet regulatory standards and performance benchmarks (Taheri *et al*. 2019, Mehrabi *et al*. 2021a). Educationally, modeling nurtures problem-solving skills and analytical thinking (Firouzianhaji *et al*. 2021, Mehrabi *et al*. 2021b). Overall, modeling is not just a technical necessity—it's a cornerstone of engineering excellence (Toghroli *et al*. 2020, Mehrabi *et al*. 2024, Mehrabi *et al*. 2025).

The present work explores the vibrational behavior and mechanical enhancement of curved concrete shell panels embedded with nano-alumina reinforcements. By leveraging the superior properties of nanomaterials, particularly nano-alumina, the study aims to improve the structural integrity and dynamic performance of concrete elements subjected to complex boundary conditions. A detailed parametric analysis is performed to evaluate the effects of nanoparticle distribution patterns, shell geometry (expressed via thickness-to-length and radius-to-length ratios), and elastic foundation characteristics modeled by Winkler and Pasternak parameters. The concept of relative frequency change is introduced as a metric to assess the sensitivity of natural frequencies under these varying conditions. Results indicate a clear trend of frequency enhancement with increasing nano-alumina content, especially when strategically distributed. The findings also confirm the substantial influence of foundation stiffness on vibrational responses, with stiffer foundations yielding higher natural frequencies. Comparative evaluations with classical plate theory and Reddy's higher-order shear deformation theory validate the proposed methodology, confirming its accuracy and robustness. This research underscores the potential of nano-engineered materials in advancing structural performance and opens new pathways for smart, vibration-resistant concrete systems in modern infrastructure.

2. Mathematical modeling

2.1 Material properties formulations of nano-Alumina

Nano-Alumina (nAl_2O_3) significantly enhances the mechanical properties of concrete, including compressive strength, tensile capacity, and durability. Its high surface area and reactivity improve the matrix-reinforcement bonding, resulting in better stress transfer and crack resistance. Due to its nanoscale size, nAl_2O_3 fills microvoids and refines the pore structure, leading to

improved density and reduced permeability. This makes concrete more resistant to aggressive environments, such as freeze-thaw cycles, sulfate attack, or chloride penetration. Ultimately, incorporating nano-alumina extends the service life and structural performance of concrete infrastructures while maintaining a lightweight design. The various patterns of this kind of innovative reinforcement is as follows:

$$\text{Pattern X: } V^{A}_{nAl_2O_3}(\mathfrak{A}_3) = \frac{4|\mathfrak{A}_3|}{h} V^{T}_{nAl_2O_3} \tag{1a}$$

$$\text{Pattern O: } V^{O}_{nAl_2O_3}(\mathfrak{A}_3) = \left(2 - \frac{4|\mathfrak{A}_3|}{h}\right) V^{T}_{nAl_2O_3} \tag{1b}$$

$$\text{Pattern V: } V^{V}_{nAl_2O_3}(\mathfrak{A}_3) = \left(\frac{\mathfrak{A}_3}{h} + 0.5\right) 2V^{T}_{nAl_2O_3} \tag{1c}$$

$$\text{Pattern UD: } V^{UD}_{nAl_2O_3}(\mathfrak{A}_3) = V^{T}_{nAl_2O_3} \tag{1d}$$

$$\text{Pattern A: } V^{X}_{nAl_2O_3}(\mathfrak{A}_3) = \left(1 - \frac{\mathfrak{A}_3}{h}\right) V^{T}_{nAl_2O_3} \tag{1e}$$

The geometry factor represents the shape and aspect ratio of nano-Alumina particles, which strongly influences mechanical reinforcement behavior. It is calculated using the ratio of particle diameter to thickness.

$$\xi_l = \xi_t = \frac{2d_{nAl_2O_3}}{h_{nAl_2O_3}} \tag{2}$$

These parameters capture the efficiency of reinforcement based on the stiffness mismatch between matrix and nano-alumina. They are influenced by both the mechanical properties and geometry of the particles.

$$\eta_l = \frac{\left(\frac{E_{nAl_2O_3}}{E_M} - 1\right)}{\left(\frac{E_{nAl_2O_3}}{E_M} + \xi_l\right)} \tag{3a}$$

$$\eta_t = \frac{\left(\frac{E_{nAl_2O_3}}{E_M} - 1\right)}{\left(\frac{E_{nAl_2O_3}}{E_M} + \xi_t\right)} \tag{3b}$$

These two equations compute the directional stiffness (moduli) of the nanocomposite: longitudinal (E_l) and transverse (E_t). They incorporate particle content, geometry, and matrix compatibility.

$$E_{nAl_2O_3} = 0.49E_l + 0.51E_t \tag{4a}$$

$$E_l = \frac{E_M(1 + \xi_l\eta_l V_{nAl_2O_3})}{1 - \eta_l V_{nAl_2O_3}} \tag{4b}$$

$$E_t = \frac{E_M(1 + \xi_t\eta_t V_{nAl_2O_3})}{1 - \eta_t V_{nAl_2O_3}} \tag{4c}$$

This equation gives the overall Young's modulus of the reinforced composite by combining both directional moduli. The weights (0.49 and 0.51) reflect an empirical balance derived from literature.

$$\upsilon_{nAl_2O_3} = \upsilon_M V_M + \upsilon_{nAl_2O_3} V_{nAl_2O_3}, \tag{5}$$

Poisson's ratio of the composite is computed using the rule of mixtures, weighted by volume fractions. It represents how the composite behaves under transverse strain.

Table 1 The material properties of concrete structure reinforced by nAl_2O_3

Material	Elasticity Modulus (GPa)	Mass Density (kg/m³)	Poisson's Ratio
Concrete	30	2300	0.2
Nano-Alumina	350	3900	0.22

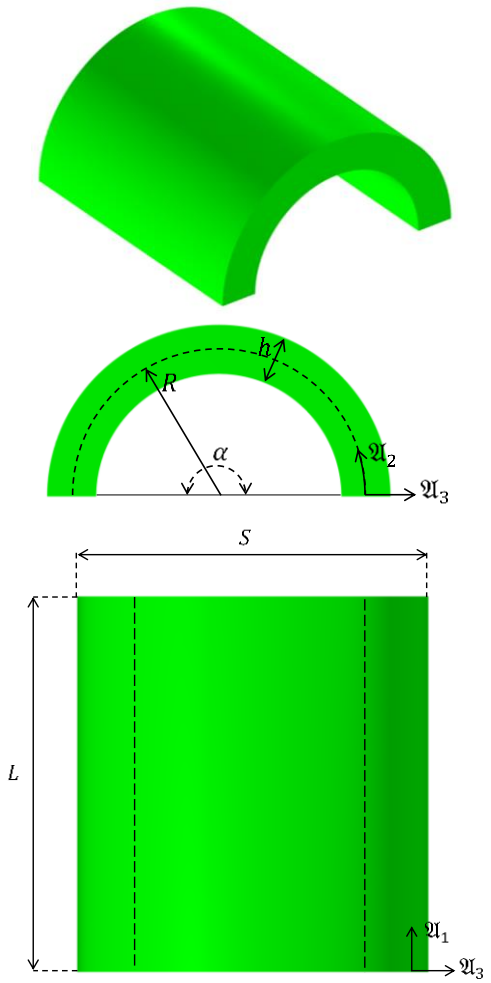

Fig. 1 Geometrical features of the cylindrical shell

$$\rho_{nAl_2O_3} = \rho_M V_M + \rho_{nAl_2O_3} V_{nAl_2O_3} \tag{6}$$

Similar to Poisson's ratio, the overall density is determined from the mass densities and volume fractions of each component. This is essential for structural and dynamic simulations.

$$V_{nAl_2O_3} + V_M = 1 \tag{7}$$

This constraint ensures volume consistency, stating that the total material is made up of matrix and reinforcement only. It anchors all other formulations to a physically meaningful system. The material properties of concrete structure reinforced by nAl_2O_3 is given in Table 1 (Lamond and Pielert 2006, Fu *et al*. 2018).

2.2 Theoretical formulations

Consider a concrete cylindrical panel as illustrated in

Fig. 1, characterized by its length L, thickness h, radius R, constant arc length S, and subtended angle β. The reference surface of the panel is defined at its mid-surface, and an orthogonal coordinate system $\mathfrak{A}_1$, $\mathfrak{A}_2$ and $\mathfrak{A}_3$ is employed for analysis. In this system, the $\mathfrak{A}_1$, $\mathfrak{A}_2$ and $\mathfrak{A}_3$ axes correspond to the axial, circumferential, and radial directions, respectively, as depicted in Fig. 1.

2.2.1 Displacement field

An arbitrary location within the displacement field of the cylindrical panel can be described based on the higher-order shear deformation theory (HSDT) as presented as follows:

$$\mathcal{U}_1(\mathfrak{A}_1,\mathfrak{A}_2,\mathfrak{A}_3,t)=u_1(\mathfrak{A}_1,\mathfrak{A}_2,t)+\mathfrak{A}_3\mathcal{F}_1(\mathfrak{A}_1,\mathfrak{A}_2,t)-\mathfrak{P}c_2\mathfrak{A}_3^3\left(\mathcal{F}_1(\mathfrak{A}_1,\mathfrak{A}_2,t)+\frac{\partial u_3(\mathfrak{A}_1,\mathfrak{A}_2,t)}{\partial\mathfrak{A}_1}\right), \tag{8a}$$

$$\mathcal{U}_2(\mathfrak{A}_1,\mathfrak{A}_2,\mathfrak{A}_3,t)=\left(1+\frac{\mathfrak{A}_3}{R}\right)u_2(\mathfrak{A}_1,\mathfrak{A}_2,t)+\mathfrak{A}_3\mathcal{F}_2(\mathfrak{A}_1,\mathfrak{A}_2,t)-\mathfrak{P}c_2\mathfrak{A}_3^3\left(\mathcal{F}_2(\mathfrak{A}_1,\mathfrak{A}_2,t)+\frac{\partial u_3(\mathfrak{A}_1,\mathfrak{A}_2,t)}{R\partial\mathfrak{A}_2}\right), \tag{8b}$$

$$\mathcal{U}_3(\mathfrak{A}_1,\mathfrak{A}_2,\mathfrak{A}_3,t)=u_3(\mathfrak{A}_1,\mathfrak{A}_2,t). \tag{8c}$$

The displacement components along the $\mathfrak{A}_1$, $\mathfrak{A}_2$, and $\mathfrak{A}_3$ directions are indicated by $\mathcal{U}_1$, $\mathcal{U}_2$ and $\mathcal{U}_3$, respectively. Time is denoted by t, while u_1, u_2 and u_3 represent the displacements at a point located on the mid-surface. The rotational components of the normal vectors to the mid-surface, relative to the $\mathfrak{A}_1$ and $\mathfrak{A}_2$ axes, are labeled as $\mathcal{F}_1$ and $\mathcal{F}_2$. Additionally, the equations corresponding to the first-order shear deformation theory (FSDT) can be obtained by setting $\mathfrak{P}=0$. Considering von Karman-type geometric nonlinearity, the strain-displacement relationships can be formulated as follows.

$$\epsilon_i=\epsilon_i^0+\mathfrak{A}_3(\beta_i^0+\mathfrak{A}_3^2\beta_i^2),\ i=1,2,6 \tag{9a}$$

$$\epsilon_j=\epsilon_j^0+\mathfrak{A}_3^2\beta_j^1,\quad j=4,5 \tag{9b}$$

where

$$\epsilon_1^0=u_{1,1}+\frac{1}{2}\left(u_{3,1}\right)^2,\quad \epsilon_2^0=\frac{1}{R}u_{2,2}+\frac{u_3}{R}+\frac{1}{2}\left(\frac{1}{R}u_{3,2}\right)^2,\ \epsilon_4^0=\mathcal{F}_2+\frac{1}{R}u_{3,2}, \tag{10a}$$

$$\epsilon_5^0=\mathcal{F}_1+u_{3,1},\ \epsilon_6^0=u_{2,1}+\frac{1}{R}u_{1,2}+\frac{1}{R}u_{3,1}u_{3,2},\ \beta_1^0=\mathcal{F}_{1,1},\ \beta_2^0=\frac{1}{R}\mathcal{F}_{2,2}, \tag{10b}$$

$$\beta_6^0=\mathcal{F}_{2,1}+\frac{1}{R}\mathcal{F}_{1,2},\ \beta_4^1=-cc_1\left(\mathcal{F}_2+\frac{1}{R}u_{3,2}\right),\ \beta_5^1=-c_1\left(\mathcal{F}_1+u_{3,1}\right), \tag{10c}$$

$$\beta_1^2=-c_2\left(\mathcal{F}_{1,1}+u_{3,11}\right),\ \beta_2^2=-c_2\left(\frac{1}{R}\mathcal{F}_{2,2}+\frac{1}{R^2}u_{3,22}\right), \tag{10d}$$

$$\beta_6^2=-c_2\left(\mathcal{F}_{2,1}+\frac{1}{R}\mathcal{F}_{1,2}+2\frac{1}{R}u_{3,12}\right). \tag{10e}$$

where $c_1=4/h^2$ and $c_2=c_1/3$.

2.3 Constitutive equations

The elastic constitutive relations for the composite cylindrical panel under a plane stress condition are expressed as follows.

$$\sigma_{11}=\mathbb{Q}_{11}\epsilon_{11}+\mathbb{Q}_{12}\epsilon_{22}, \tag{11a}$$

$$\sigma_{22}=\mathbb{Q}_{12}\epsilon_{11}+\mathbb{Q}_{22}\epsilon_{22}, \tag{11b}$$

$$\sigma_{23}=\mathbb{Q}_{44}\epsilon_{23}, \tag{11c}$$

$$\sigma_{13}=\mathbb{Q}_{55}\epsilon_{13}, \tag{11d}$$

$$\sigma_{12}=\mathbb{Q}_{66}\epsilon_{12}. \tag{11e}$$

where $\mathbb{Q}_{ij}$ represents the transformed reduced stiffness matrix which can be obtained as

$$\mathbb{Q}_{11}=\frac{E_{cnAl_2O_3}}{1-\left(\upsilon_{nAl_2O_3}\right)^2},\ \mathbb{Q}_{22}=\frac{E_{nAl_2O_3}}{1-\left(\upsilon_{nAl_2O_3}\right)^2},\ \mathbb{Q}_{12}=\frac{\upsilon_{nAl_2O_3}E_{nAl_2O_3}}{1-\left(\upsilon_{nAl_2O_3}\right)^2}, \tag{12a}$$

$$\mathbb{Q}_{44}=\frac{E_{nAl_2O_3}}{2\left(1+\upsilon_{nAl_2O_3}\right)},\ \mathbb{Q}_{55}=\frac{E_{nAl_2O_3}}{2\left(1+\upsilon_{nAl_2O_3}\right)},\ \mathbb{Q}_{66}=\frac{E_{nAl_2O_3}}{2\left(1+\upsilon_{nAl_2O_3}\right)}. \tag{12b}$$

2.4 Dynamic equations

The nonlinear dynamic equations that govern the behavior of the composite cylindrical panel are derived based on Hamilton's principle.

$$\int_{t_1}^{t_2}(\delta U+\delta V-\delta T)dt=0 \tag{13}$$

In this formulation, U and T represent the strain energy and kinetic energy, respectively, and they can be determined as follows:

$$U=\frac{1}{2}\iint_A\int_{-h/2}^{h/2}(\sigma_{11}\epsilon_{11}+\sigma_{22}\epsilon_{22}+\sigma_{12}\epsilon_{12}+\sigma_{13}\epsilon_{13}+\sigma_{23}\epsilon_{23})d\mathfrak{A}_3dA. \tag{14a}$$

$$T=\frac{1}{2}\iint_A\int_{-h/2}^{h/2}\rho_{nAl_2O_3}(\mathfrak{A}_3)\left(\dot{\mathcal{U}}_1^2+\dot{\mathcal{U}}_2^2+\dot{\mathcal{U}}_3^2\right)d\mathfrak{A}_3dA. \tag{14b}$$

Here, a superimposed dot denotes differentiation with respect to time. The variation in the work performed by the Winkler-Pasternak foundation can be derived using the following expressions:

$$V_1=\frac{1}{2}\iint_A\left(K_{wo}(\mathfrak{A}_1,\mathfrak{A}_2)u_3-\frac{\partial}{\partial\mathfrak{A}_1}\left(K_{\mathrm{po}}(\mathfrak{A}_1,\mathfrak{A}_2)\frac{\partial u_3}{\partial\mathfrak{A}_1}\right)- \tag{15}$$

$$\frac{1}{R^2}\frac{\partial}{\partial \mathfrak{A}_2}\left(K_{\mathrm{po}}(\mathfrak{A}_1,\mathfrak{A}_2)\frac{\partial \mathcal{u}_3}{\partial \mathfrak{A}_2}\right)\mathcal{u}_3\, dA.$$

For Exponential elastic foundation

$$K_{\mathrm{wo}}(\mathfrak{A}_1,\mathfrak{A}_2) = K_w \times \left(1+exp\left(\frac{\mathfrak{A}_1}{L}\right)\right)\times\left(1+exp\left(\frac{\mathfrak{A}_2}{\beta}\right)\right), \quad (16a)$$

$$K_{\mathrm{po}}(\mathfrak{A}_1,\mathfrak{A}_2) = K_p \times \left(1+exp\left(\frac{\mathfrak{A}_1}{L}\right)\right)\times\left(1+exp\left(\frac{\mathfrak{A}_2}{\beta}\right)\right). \quad (16b)$$

Utilizing Hamilton's principle, the nonlinear dynamic governing equations (Eqs. 17a-e) are derived through a series of mathematical operations, including the application of the Green-Gauss theorem to eliminate the gradients of virtual displacements (Khdeir *et al*. 1989).

$$\delta \mathcal{u}_1 : \mathcal{N}_{1,1} + \frac{1}{R}\mathcal{N}_{6,2} = \bar{\mathcal{I}}_1\ddot{\mathcal{u}}_1 + \bar{\mathcal{I}}_2\ddot{\mathcal{F}}_1 - \mathfrak{P}\bar{\mathcal{I}}_3\ddot{\mathcal{u}}_{3,1}, \quad (17a)$$

$$\delta \mathcal{u}_2 : \mathcal{N}_{6,1} + \frac{1}{R}\mathcal{N}_{2,2} = \bar{\mathcal{I}}_1'\ddot{\mathcal{u}}_2 + \bar{\mathcal{I}}_2'\ddot{\mathcal{F}}_2 - \frac{\mathfrak{P}}{R}\bar{\mathcal{I}}_3'\ddot{\mathcal{u}}_{3,2}, \quad (17b)$$

$$\begin{aligned}\delta \mathcal{u}_3 : \mathcal{Q}_{1,1} + \frac{1}{R}\mathcal{Q}_{2,2} - \mathfrak{P}c_1\left(\mathcal{L}_{1,1}+\frac{1}{R}\mathcal{L}_{2,2}\right) + \mathfrak{P}c_2\left(\mathcal{P}_{1,11}+\right.\\ \left.\frac{1}{R^2}\mathcal{P}_{2,22}+\frac{2}{R}\mathcal{P}_{6,12}\right) - \frac{1}{R}\mathcal{N}_2 - K_w(\mathfrak{A}_1,\mathfrak{A}_2)\mathcal{u}_3 +\\ \frac{\partial}{\partial \mathfrak{A}_1}\left(K_{\mathrm{p}}(\mathfrak{A}_1,\mathfrak{A}_2)\frac{\partial \mathcal{u}_3}{\partial \mathfrak{A}_1}\right) + \frac{1}{R^2}\frac{\partial}{\partial \mathfrak{A}_2}\left(K_{\mathrm{p}}(\mathfrak{A}_1,\mathfrak{A}_2)\frac{\partial \mathcal{u}_3}{\partial \mathfrak{A}_2}\right) =\\ \mathfrak{P}\left(\bar{\mathcal{I}}_3\ddot{\mathcal{u}}_{1,1} + \bar{\mathcal{I}}_5\ddot{\mathcal{F}}_{1,1} + \frac{\bar{\mathcal{I}}_3'}{R}\ddot{\mathcal{u}}_{2,2} + \frac{\bar{\mathcal{I}}_5'}{R}\ddot{\mathcal{F}}_{2,2} - c_2^2\mathcal{I}_7\left(\ddot{\mathcal{u}}_{3,11}+\right.\right.\\ \left.\left.\frac{1}{R^2}\ddot{\mathcal{u}}_{3,22}\right)\right) + \mathcal{I}_1\ddot{\mathcal{u}}_3,\end{aligned} \quad (17c)$$

$$\begin{aligned}\delta \mathcal{F}_1 : \mathcal{M}_{1,1} + \frac{1}{R}\mathcal{M}_{6,2} - \mathcal{Q}_1 + \mathfrak{P}c_1\mathcal{L}_1 - \mathfrak{P}c_2\left(\mathcal{P}_{1,1}+\right.\\ \left.\frac{1}{R}\mathcal{P}_{6,2}\right) = \bar{\mathcal{I}}_2\ddot{\mathcal{u}}_1 + \bar{\mathcal{I}}_4\ddot{\mathcal{F}}_1 - \mathfrak{P}\bar{\mathcal{I}}_5\ddot{\mathcal{u}}_{3,1},\end{aligned} \quad (17d)$$

$$\begin{aligned}\delta \mathcal{F}_2 : \mathcal{M}_{6,1} + \frac{1}{R}\mathcal{M}_{2,2} - \mathcal{Q}_2 + \mathfrak{P}c_1\mathcal{L}_2 - \mathfrak{P}c_2\left(\mathcal{P}_{6,1}+\right.\\ \left.\frac{1}{R}\mathcal{P}_{2,2}\right) = \bar{\mathcal{I}}_2'\ddot{\mathcal{u}}_2 + \bar{\mathcal{I}}_4'\ddot{\mathcal{F}}_2 - \frac{\mathfrak{P}}{R}\bar{\mathcal{I}}_5'\ddot{\mathcal{u}}_{3,2},\end{aligned} \quad (17e)$$

where the stress resultants are evaluated using the following expressions:

$$(\mathcal{N}_i,\mathcal{M}_i,\mathcal{P}_i) = \int_{-h/2}^{h/2} \sigma_i(1,\mathfrak{A}_3,\mathfrak{A}_3^3)d\mathfrak{A}_3, \ = 1,2,6 \quad (18a)$$

$$(\mathcal{Q}_1,\mathcal{L}_1) = \int_{-h/2}^{h/2} \sigma_5(1,\mathfrak{A}_3^2)d\mathfrak{A}_3, \quad (18b)$$

$$(\mathcal{Q}_2,\mathcal{L}_2) = \int_{-h/2}^{h/2} \sigma_4(1,\mathfrak{A}_3^2)d\mathfrak{A}_3. \quad (18c)$$

The relationship between stress resultants and strains is defined through the following constitutive equations (Reddy and Liu 1985)

$$\mathcal{N}_i = \mathcal{a}_{ij}\epsilon_j^0 + \mathcal{b}_{ij}\beta_j^0 + \mathfrak{P}e_{ij}\beta_j^2, \quad (19a)$$

$$\mathcal{M}_i = \mathcal{b}_{ij}\epsilon_j^0 + \mathcal{d}_{ij}\beta_j^0 + \mathfrak{P}\mathcal{f}_{ij}\beta_j^2, \quad (19b)$$

$$\mathcal{P}_i = e_{ij}\epsilon_j^0 + \mathcal{f}_{ij}\beta_j^0 + \mathcal{h}_{ij}\beta_j^2, \quad (19c)$$

$$\mathcal{Q}_2 = \mathcal{a}_{4j}\epsilon_j^0 + \mathfrak{P}\mathcal{d}_{4j}\beta_j^1, \quad (19d)$$

$$\mathcal{Q}_1 = \mathcal{a}_{5j}\epsilon_j^0 + \mathfrak{P}\mathcal{d}_{5j}\beta_j^1, \quad (19e)$$

$$K_2 = \mathcal{d}_{4j}\epsilon_j^0 + \mathcal{f}_{4j}\beta_j^1, \quad (19f)$$

$$K_1 = \mathcal{d}_{5j}\epsilon_j^0 + \mathcal{f}_{5j}\beta_j^1. \quad (19g)$$

where i, j = 1,2,6 and the inertias $\bar{\mathcal{I}}_i$ and $\bar{\mathcal{I}}_i'$ (i = 1, 2, 3, 4, 5) are defined by the following equations

$$\bar{\mathcal{I}}_1 = \mathcal{I}_1,\ \bar{\mathcal{I}}_1' = \mathcal{I}_1 + \mathfrak{P}\frac{2}{R}\mathcal{I}_2, \quad (20a)$$

$$\bar{\mathcal{I}}_2 = \mathcal{I}_2 - \mathfrak{P}c_2\mathcal{I}_4,\ \bar{\mathcal{I}}_2' = \mathcal{I}_2 + \mathfrak{P}\left(\frac{\mathcal{I}_3}{R} - c_2\left(\mathcal{I}_4+\frac{\mathcal{I}_5}{R}\right)\right), \quad (20b)$$

$$\bar{\mathcal{I}}_3 = c_2\mathcal{I}_4,\ \bar{\mathcal{I}}_3' = c_2\left(\mathcal{I}_4+\frac{\mathcal{I}_5}{R}\right), \quad (20c)$$

$$\bar{\mathcal{I}}_4 = \mathcal{I}_3 - \mathfrak{P}c_2(2\mathcal{I}_5 - c_2\mathcal{I}_7),\ \bar{\mathcal{I}}_4' = \mathcal{I}_4, \quad (20d)$$

$$\bar{\mathcal{I}}_5 = c_2(\mathcal{I}_5 - c_2\mathcal{I}_7),\ \bar{\mathcal{I}}_5' = \bar{\mathcal{I}}_5, \quad (20e)$$

$$(\mathcal{I}_1,\mathcal{I}_2,\mathcal{I}_3,\mathcal{I}_4,\mathcal{I}_5,\mathcal{I}_7) = \int_{-h/2}^{h/2} \rho_{nAl_2O_3}(\mathfrak{A}_3)(1,\mathfrak{A}_3,\mathfrak{A}_3^2,\mathfrak{A}_3^3,\mathfrak{A}_3^4,\mathfrak{A}_3^6)d\mathfrak{A}_3. \quad (20f)$$

3. Solution procedure

3.1 A brief of NURBS-based isogeometric analysis

Isogeometric Analysis (IGA) is grounded in the isoparametric concept, which advocates using identical basis functions for both the geometric representation and the discretization of unknown field variables. In IGA, the commonly used basis functions are NURBS (Non-Uniform Rational B-Splines), which are formed by a weighted combination of B-splines. Extensive discussions on B-splines and NURBS can be found in existing literature, however, a few essential aspects are summarized below for completeness.

3.2 A brief of B-spline and NURBS basis functions

A non-decreasing knot vector, denoted as $\mathbf{\Pi} = \{\mathbb{a}_1, \mathbb{a}_2, \dots, \mathbb{a}_{n+p+1}\}$ can be introduced in the parametric domain, where each $\mathbb{a}_i$ represents a knot value with $i = 1, \dots, n+p$. Here, n indicates the number of basis functions, and p is the polynomial degree of the basis functions. A knot vector is termed 'open' if its first and last knot values appear $\mathrm{p}+1$ times. The continuity of a B-spline basis function is c^{∞} within a knot span, c^{p-1} at a simple knot, and c^{p-k} at a knot of multiplicity k. The B-spline basis functions of degree $p = 0$ are defined using the Cox-de Boor recursion formula as follows:

$$\mathcal{N}_{i,0}(\mathbb{a}) = \begin{cases} 1 & \text{if } \mathbb{a}_i \le \mathbb{a} \le \mathbb{a}_{i+1} \\ 0 & \text{otherwise} \end{cases} \quad (21)$$

and the order $\mathrm{p} \ge 1$ B-spline basis functions are specified as

$$\begin{aligned}\mathcal{N}_{i,p}(\mathbb{a}) = \frac{\mathbb{a}-\mathbb{a}_i}{\mathbb{a}_{i+p}-\mathbb{a}_i}\mathcal{N}_{i,p-1}(\mathbb{a})\\ + \frac{\mathbb{a}_{i+p+1}-\mathbb{a}}{\mathbb{a}_{i+p+1}-\mathbb{a}_{i+1}}\mathcal{N}_{i+1,p-1}(\mathbb{a})\end{aligned} \quad (22)$$

Following this, the derivatives of B-spline basis functions can be computed recursively, starting from lower-order derivatives. The first-order derivative of a B-spline

basis function is given by:

$$\frac{\mathrm{d}}{\mathrm{d}\mathbb{a}}\mathcal{N}_{i,p}(\mathbb{a}) = \frac{p}{\mathbb{a}_{i+p}-\mathbb{a}_i}\mathcal{N}_{i,p-1}(\mathbb{a}) - \frac{p}{\mathbb{a}_{i+p+1}-\mathbb{a}_{i+1}}\mathcal{N}_{i+1,p-1}(\mathbb{a}) \tag{23}$$

and the derivative of kth order is given as

$$\frac{\mathrm{d}^k}{\mathrm{d}\mathbb{a}^k}\mathcal{N}_{i,p}(\mathbb{a}) = \frac{p}{\mathbb{a}_{i+p}-\mathbb{a}_i}\left(\frac{\mathrm{d}^{k-1}}{\mathrm{d}\mathbb{a}^{k-1}}\mathcal{N}_{i,p-1}(\mathbb{a})\right) - \frac{p}{\mathbb{a}_{i+p+1}-\mathbb{a}_{i+1}}\left(\frac{\mathrm{d}^{k-1}}{\mathrm{d}\mathbb{a}^{k-1}}\mathcal{N}_{i+1,p-1}(\mathbb{a})\right) \tag{24}$$

Two-dimensional B-spline basis functions in the parametric coordinates ξ and $\mathcal{B}$ can be constructed by taking the tensor product of B-splines defined in the $\mathbb{a}$ and $\mathcal{B}$-directions, using two corresponding knot vectors $\mathbf{\Pi} = \{\mathbb{a}_1, \mathbb{a}_2, \dots, \mathbb{a}_{n+p+1}\}$ and $\mathbf{\Sigma} = \{\mathbb{b}_1, \mathbb{b}_2, \dots, \mathbb{b}_{m+q+1}\}$.

$$\mathcal{N}_A(\mathbb{a},\mathbb{b}) = \mathcal{N}_{i,p}(\mathbb{a})\mathcal{M}_{j,q}(\mathbb{b}) \tag{25}$$

Here, the jth B-spline basis function of order q in the η-direction is represented by $\mathcal{M}_{j,q}(\mathbb{b})$.

3.3 Discrete equations based on NURBS approximations

By using the previously defined NURBS basis functions, the displacement field in the composite cylindrical panel can be approximated as follows:

$$\boldsymbol{u}^h(\mathbb{a},\mathbb{b}) = \sum_{A=1}^{n\times m} R_A(\mathbb{a},\mathbb{b})\mathbb{q}_A \tag{26}$$

Here, $\mathbb{q}_A$ represents the vector of nodal degrees of freedom (DOFs) associated with control point A, and $n \times m$ indicates the total number of NURBS basis functions.

$$\mathbb{q}_A = \{u_{1A}u_{2A}u_{3A}\mathcal{F}_{1A}\mathcal{F}_{2A}\}^{\mathrm{T}} \tag{27}$$

The strain-displacement relation that arises from substituting Eq. (26) into Eqs. (9a) and (9b) is as follows:

$$\boldsymbol{\epsilon} = \sum_{A=1}^{ncP}(\mathfrak{B}_A^L + \frac{1}{2}\mathfrak{B}_A^{NL})\mathbb{q}_A \tag{28}$$

The symbols $\mathfrak{B}_A^L$ and $\mathfrak{B}_A^{NL}$ represent the linear infinitesimal strain matrix and the nonlinear strain matrix, respectively. Consequently, the discrete equations that govern the high-amplitude free vibrations of composite cylindrical panels can be derived as follows:

$$[\mathbb{k}_L + \mathbb{k}_{NL1}(\mathbb{q}) + \mathbb{k}_{NL2}(\mathbb{q})]\mathbb{q} + \mathbb{m}\ddot{\mathbb{q}} = \mathbf{0} \tag{29}$$

In this context, $\mathbb{q}$ denotes the global displacement vector, mmm represents the global mass matrix, and $\mathbb{k}_{NL1}$ and $\mathbb{k}_{NL2}$ correspond to the global nonlinear stiffness matrices, exhibiting quadratic and linear dependence on $\mathbb{q}$, respectively. The global linear stiffness matrix is indicated by $\mathbb{k}_L$. To analyze the relationship between the nonlinear frequency ratio and vibration amplitude in a harmonic vibration scenario, the unknown displacement vector can be formulated as:

$$\mathbb{q} = \mathbb{q}^*\sin(\omega t) \tag{30}$$

The vector $\mathbb{q}^*$ signifies the nonlinear mode shape, while ω denotes the natural frequency of vibration. By inserting Eq. (30) into Eq. (29), the resulting residual expression is derived as follows:

$$\mathbf{R} = (\mathbb{k}_L + \mathbb{k}_{NL1}\sin(\omega t) + \mathbb{k}_{NL2}\sin^2(\omega t))\mathbb{q}^*\sin\omega t - \omega^2\mathbb{m}\mathbb{q}^*\sin(\omega t) \tag{31}$$

The time parameter is removed using the Galerkin weighted residual approach, i.e.

$$\int_0^{\pi/(2\omega)}\mathbf{R}\sin(\omega t)\mathrm{d}t = 0, \tag{32}$$

Consequently, the nonlinear eigenvalue problem characterizes the large-amplitude vibrations of the composite cylindrical panel within the frequency domain as follows:

$$(\mathbb{k}_L + \frac{8}{3\pi}\mathbb{k}_{NL1} + \frac{3}{4}\mathbb{k}_{NL2} - \omega^2\mathbb{m})\mathbb{q}^* = 0 \tag{33}$$

Eq. (33) can be approached as an eigenvalue problem. By removing the nonlinear terms $\mathbb{k}_{NL1}$ and $\mathbb{k}_{NL2}$, a linear eigenvalue equation is obtained. This allows the determination of the primary eigenvalue—representing the fundamental frequency—and its associated eigenvector, which corresponds to the vibration mode. To incorporate a specific transverse displacement, the vibration mode is scaled accordingly, enabling the computation of the updated nonlinear stiffness matrices $\mathbb{k}_{NL1}$ and $\mathbb{k}_{NL2}$. The revised eigenvalue problem is then solved to obtain a new eigenvalue (nonlinear frequency) and its corresponding mode shape. This iterative process is repeated until the relative difference between successive eigenvalue vectors falls below the specified tolerance—set at 10^{-5} in this study. Additionally, the dimensionless parameters are defined as follows:

$$K_W^* = \frac{K_W R^5}{E_m I},\ K_P^* = \frac{K_P R^3}{E_m I},\ \bar{\omega} = \omega\sqrt{\frac{\rho_m}{E_m}} \tag{34}$$

The relative frequency change (RFC) in this work can be formulated as follows:

$$RFC = \frac{\omega_1 - \omega_2}{\omega_2} \tag{35}$$

where ω_1 and ω_2 are natural frequency of the structure with and without nanocomposite reinforcement.

4. Result

4.1 Validation with nondestructive testing

Table 2 presents a benchmark comparison of non-dimensional natural frequencies for the first six vibration modes of a cylindrical panel with simply supported edges, using three theoretical models: the present model (likely higher-order or refined), Classical Plate Theory (CPT), and Reddy's Third-Order Shear Deformation Theory (TSDT).

Table 2 A comparative analysis conducted for the first six nondimensional frequency parameters $\left(\bar{\omega} = r_0\sqrt{\rho/E}\right)$ of cylindrical panels under various boundary condition configurations $\left(\alpha = 90°, r_0 = R + \frac{h}{2}, L/r_0 = 1.5, r_0/h = 100, E = 210\ \text{GPa}, \nu = 0.3, \rho = 7800\text{kg/m}^3,\ SSSS\right)$

Method	$\bar{\omega}_1$	$\bar{\omega}_2$	$\bar{\omega}_3$	$\bar{\omega}_4$	$\bar{\omega}_5$	$\bar{\omega}_6$
Present	0.24250	0.25641	0.34229	0.38532	0.39243	0.42000
Classical plate theory (Arani *et al*. 2021)	0.24450	0.25813	0.34741	0.38647	0.39623	0.42883
Reddy's third-order shear deformation theory (Akbari *et al*. 2022)	0.24483	0.25809	0.34319	0.38708	0.39442	0.41824

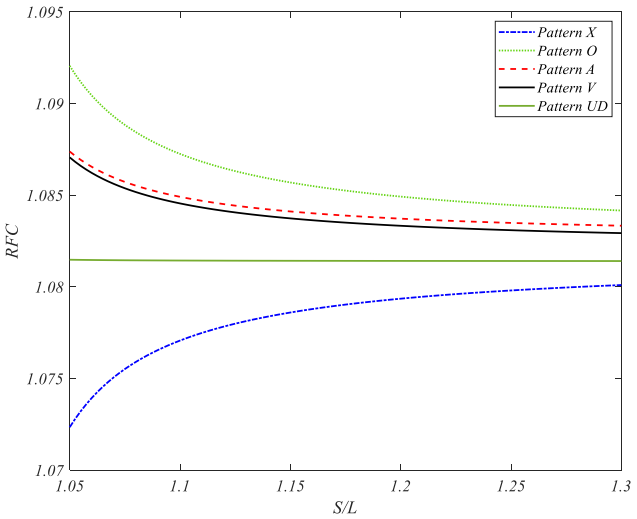

Fig. 2 The influence of various nano-alumina reinforcement distribution patterns on the RFC of a curved concrete cylindrical panel as a function of the normalized arc length

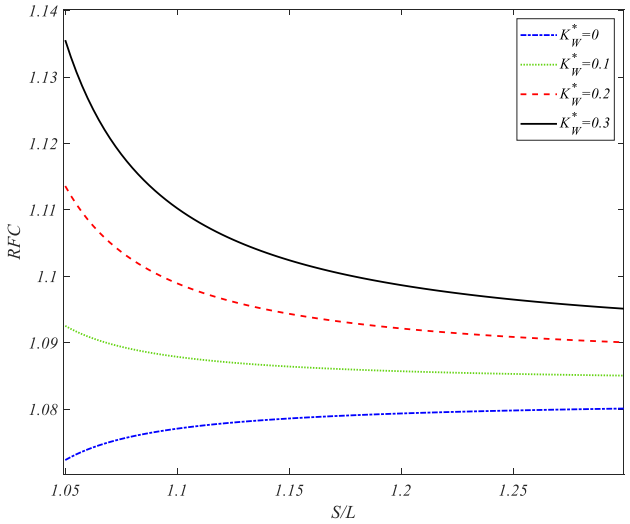

Fig. 3 The impact of the dimensionless Winkler foundation stiffness parameter on the RFC of the curved concrete panel, plotted against *S/L*

The present model consistently predicts slightly lower values for all six modes compared to CPT and TSDT, with maximum differences occurring in higher modes. This behavior reflects the greater accuracy of the present approach in capturing the effect of transverse shear deformation, especially at higher frequencies. While CPT tends to over-estimate natural frequencies due to its neglect of shear effects, TSDT provides closer agreement with the present model, particularly from the third mode onward. The alignment across all models validates the reliability of the present method while also highlighting its improved predictive capability in complex shell structures reinforced with nano-materials.

4.2 Parametric results

Fig. 2 explores the influence of various nano-alumina reinforcement distribution patterns on the RFC of a curved concrete cylindrical panel as a function of the normalized arc length (S/L). Patterns A, O, V, X and UD (uniform distribution) are compared. The results indicate that Pattern V and Pattern O consistently lead to higher RFC values compared to other configurations, reflecting their superior reinforcement effectiveness in dynamic performance. onversely, Pattern X yields the lowest RFC, suggesting a less favorable vibration behavior. Notably, as S/L increases, the RFC for Pattern X exhibits an increasing trend, while C the others show slight decreasing or plateauing behavior. These variations underscore the critical role that nano-alumina spatial distribution plays in tuning the mechanical vibrational response of nano-modified concrete shells. Selecting an optimal reinforcement pattern can significantly enhance structural dynamics, especially in curved geometries where localized stiffness variations are more influential.

Fig. 3 demonstrates the impact of the dimensionless Winkler foundation stiffness parameter on the RFC of the curved concrete panel, plotted against S/L. As the foundation stiffness increases from $K_W^* = 0.3$, the RFC experiences a consistent and substantial elevation. This behavior is attributed to the enhanced elastic support provided by the Winkler foundation, which increases the overall system stiffness and thereby elevates natural frequency responses. The influence of K_W^* is particularly significant at lower values of S/L, where curvature effects dominate. As S/L increases, the RFC converges across all values of K_W^*, suggesting that the role of foundation stiffness diminishes with larger arc lengths. This insight is valuable in foundation design, especially for curved panels in contact with elastic media, as tailored foundation parameters can effectively modify vibrational characteristics.

Fig. 4 assesses how varying the Pasternak foundation parameter affects the RFC across a range of normalized are lengths. The Pasternak model extends the Winkler approach by incorporating shear interaction within the foundation, offering a more comprehensive simulation of subgrade

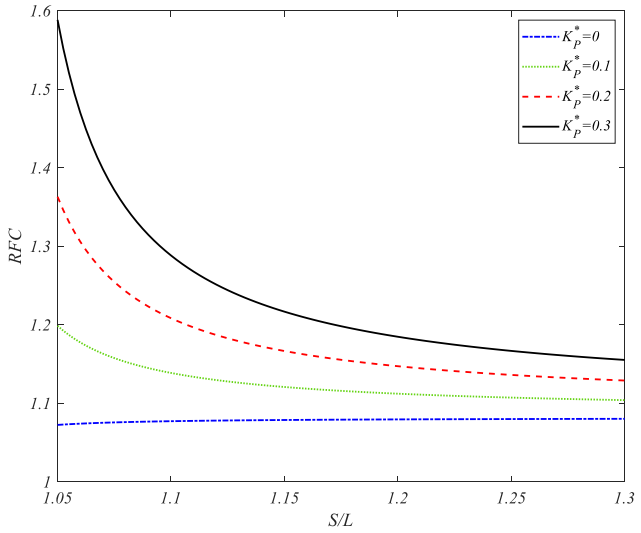

Fig. 4 The influence of Pasternak foundation parameter on the RFC across a range of normalized arc lengths

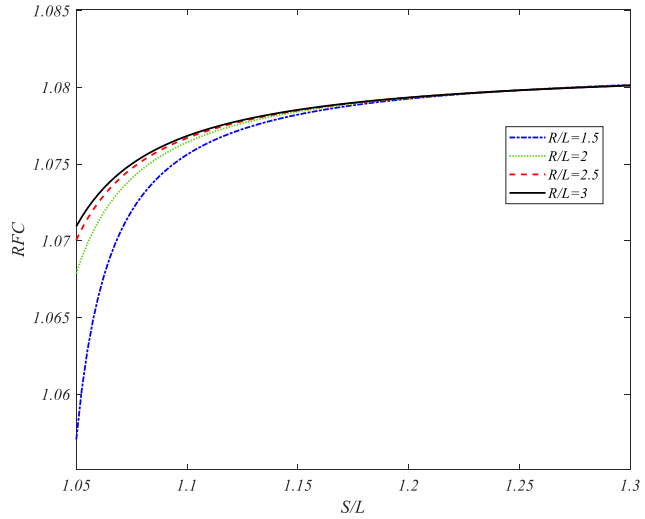

Fig. 5 The role of geometrical curvature, expressed through the radius-to-length ratio, on the RFC of the nano-reinforced cylindrical panel

reactions. As shown, increasing K_P^* leads to a pronounced rise in RFC, especially at lower S/L values. For instance, at $K_P^* = 0.3$, the RFC reaches nearly 1.6, indicating a marked enhancement in vibrational response due to shear coupling within the substructure. This effect diminishes with increasing arc length, echoing the behavior seen with the Winkler foundation. The results highlight that shear modulus inclusion significantly amplifies the dynamic stiffness, making the Pasternak model a more sensitive and effective foundation representation when analyzing advanced concrete shell structures under nano-reinforcement.

Fig. 5 examines the role of geometrical curvature, expressed through the radius-to-length ratio, on the RFC of the nano-reinforced cylindrical panel. Multiple values of R/L (1.5 to 3) are compared over increasing arc length ratios. The results reveal that as R/L increases (i.e., the shell becomes flatter), the RFC slightly rises and eventually stabilizes across all S/L values. This indicates a reduction

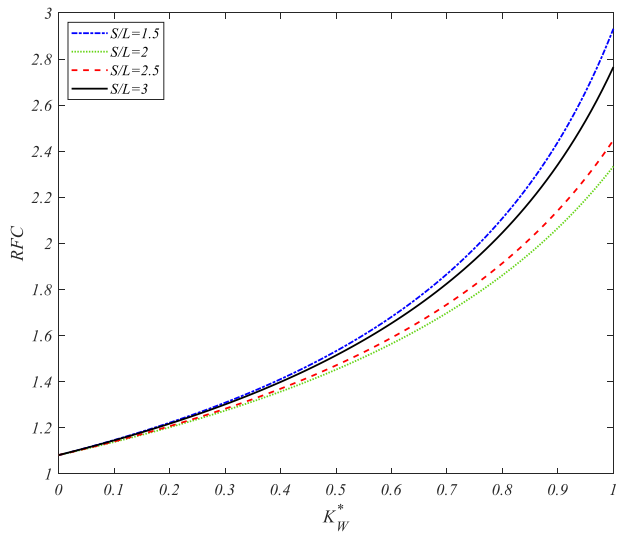

Fig. 6 The variation of the RFC as a function of the dimensionless Winkler foundation parameter, for different arc-length ratios

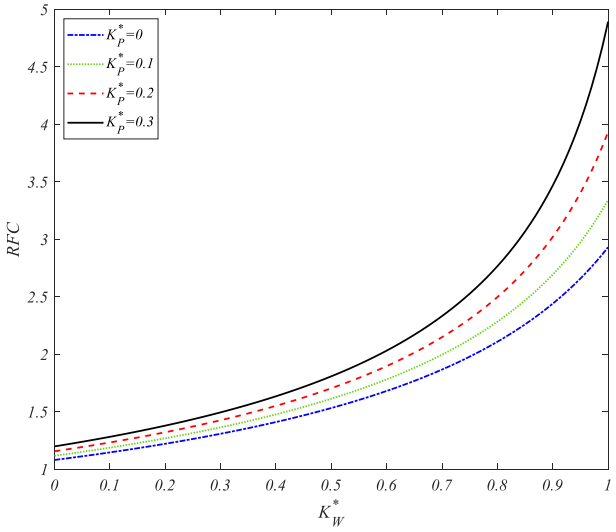

Fig. 7 The combined influence of the Winkler foundation stiffness and the Pasternak shear interaction parameter on RFC

in curvature-induced stiffness, yielding a more uniform vibrational response. The most significant changes in RFC occur at low S/L, where curvature effects are strongest. The converging trend as S/L increases suggests a dominant role of arc length over curvature in governing dynamic behavior in elongated panels. These findings underscore the need to consider geometrical nonlinearities in vibration analysis, particularly for highly curved shells where curvature radius significantly interacts with material and foundation properties.

Fig. 6 illustrates the variation of the RFC as a function of the dimensionless Winkler foundation parameter, for different arc-length ratios. As the stiffness of the Winkler foundation increases, RFC experiences a significant nonlinear rise, highlighting the substantial influence of elastic support on vibrational behavior. For each value of

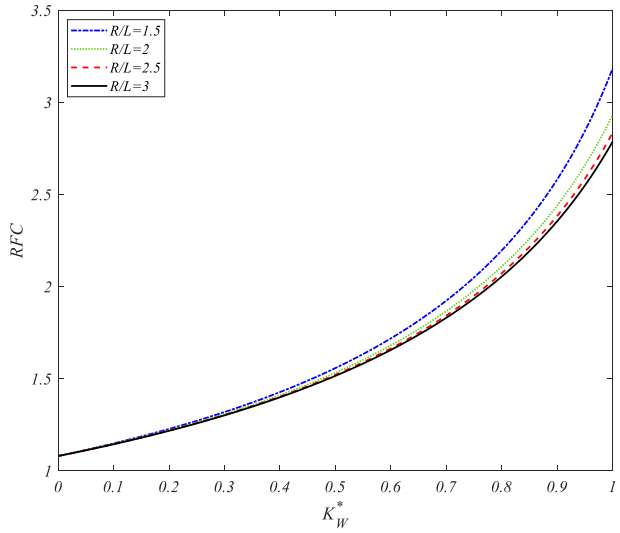

Fig. 8 The variation of RFC with increasing Winkler foundation stiffness, across different values of the radius-to-length ratio

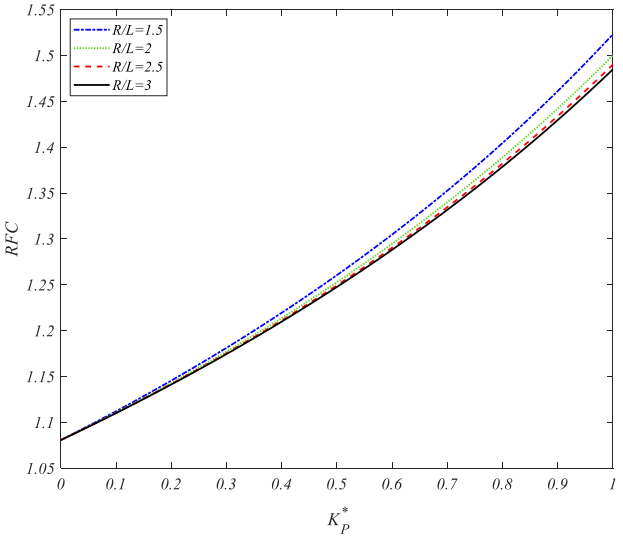

Fig. 9 The variation of RFC with increasing K_P^*, across different values of the radius-to-length ratio

K_W^*, lower arc-length ratios (e.g., S/L=1.5) consistently exhibit higher RFC values, implying a stiffer dynamic response due to the shorter arc and increased geometric curvature. In contrast, elongated panels (S/L=3) show reduced sensitivity, suggesting geometric flexibility offsets foundation effects. This relationship suggests that panels with reduced arc length and supported by stiffer elastic media are more dynamically responsive. These insights support optimization of curved shell designs in structural systems requiring controlled frequency characteristics, particularly through adjustment of arc geometry and subgrade stiffness.

Fig. 7 analyzes the combined influence of the Winkler foundation stiffness and the Pasternak shear interaction parameter on RFC. For each fixed value of K_P^*, the RFC increases monotonically with increasing K_W^*. However, the inclusion of shear interaction significantly amplifies this

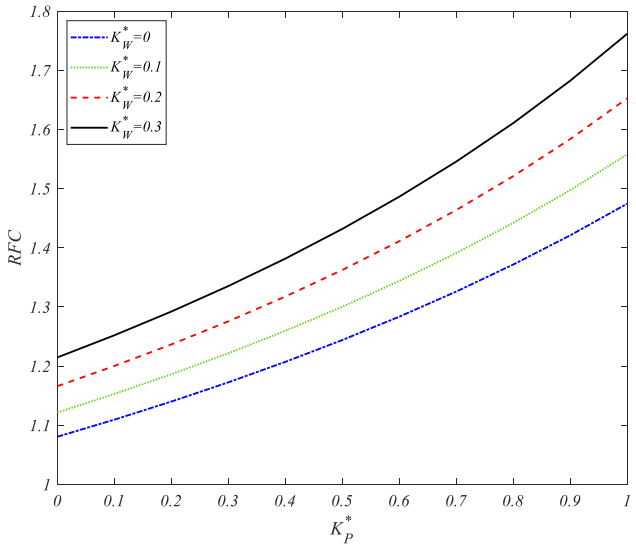

Fig. 10 The variation in relative frequency change with respect to the dimensionless Pasternak foundation parameter, for different levels of the dimensionless Winkler foundation parameter

effect. Notably, the curve corresponding to K_P^*=0.3 yields the highest RFC at each value of K_W^*, with RFC reaching up to 4.5 when K_W^* =1. The results emphasize the compound enhancement in vibrational response when both vertical and shear foundation stiffness are considered. At low K_W^*, the differences among curves are minimal, but diverge rapidly at higher stiffness values, underscoring the nonlinear coupling between foundation types. These findings advocate for the Pasternak foundation model in precision structural design, where subtle shear-support interactions can markedly influence dynamic performance.

Fig. 8 presents the variation of RFC with increasing Winkler foundation stiffness, across different values of the radius-to-length ratio. As expected, all curves demonstrate a strong, nearly exponential increase in RFC with K_W^*, indicative of rising system stiffness and natural frequency. However, geometric curvature, represented by R/L, modulates this trend. Panels with smaller curvature (higher R/L) show slightly reduced RFC values, indicating lower vibrational sensitivity. In contrast, highly curved shells (e.g., R/L =1.5) display a more pronounced response. These differences, though subtle, highlight the impact of geometry in conjunction with foundation support on dynamic characteristics. Importantly, the converging behavior at low K_W^* and diverging behavior at higher values suggest a geometric amplification of foundation effects in stiffer subgrade conditions. This finding informs design considerations for nano-modified concrete shells requiring specific vibrational performance through curvature control.

This subfigure investigates how curvature, defined by the radius-to-length ratio, affects the RFC with respect to the Pasternak foundation paramete. Across all values of R/L, RFC increases steadily and nonlinearly with increasing increasing K_P^*, indicating that the inclusion of shear interaction in the foundation significantly enhances vibrational stiffness. The effect is consistent regardless of

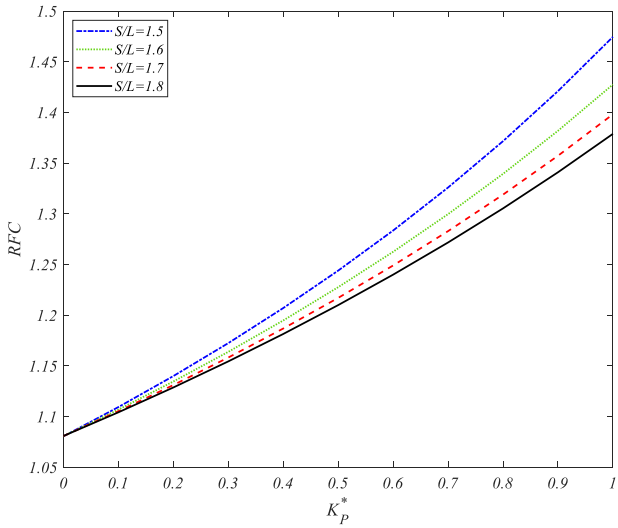

Fig. 11 The influence of shell geometry—specifically the arc length to total length ratio—on RFC as a function of K_P^*

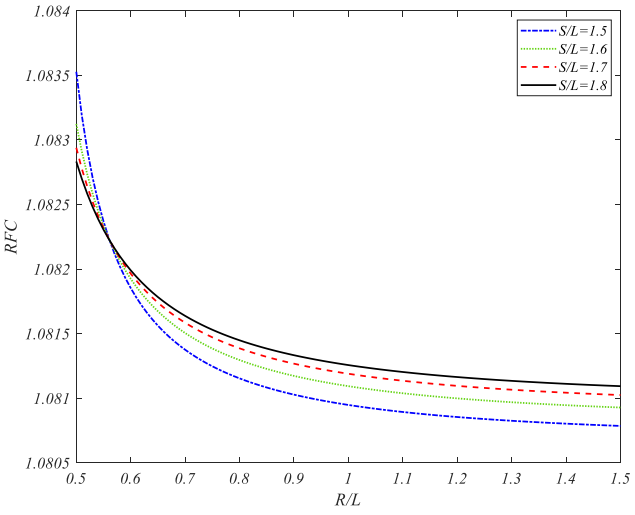

Fig. 12 The relationship between the radius-to-length ratio and RFC for varying arc length-to-length ratios

shell geometry, though curvature-induced differences are observed: the most curved shell (R/L=1.5) demonstrates slightly higher RFCs at all K_P^* values compared to flatter shells. This suggests that the geometric stiffness inherent in curved panels synergizes with shear foundation reactions, amplifying the vibrational frequency shift. The modest divergence between curves implies that while curvature plays a secondary role to foundation shear in influencing RFC, its influence remains non-negligible in high-performance structural optimization. The results reinforce the need to jointly consider geometry and foundation modeling in concrete nanocomposite vibration design.

Fig. 10 presents the variation in relative frequency change with respect to the dimensionless Pasternak foundation parameter, for different levels of the dimensionless Winkler foundation parameter. The results show a consistently increasing trend in RFC as K_P^* increases, which is more pronounced at higher K_W^* values. This indicates a synergistic effect of the foundation parameters on the vibrational response of the nano-reinforced cylindrical concrete shell. The enhancement in RFC reflects improved stiffness characteristics due to the dual elastic foundation, underscoring the role of subgrade modeling in nano-modified structural systems. The curved shell, reinforced with nano-alumina, demonstrates that mechanical vibration resistance can be finely tuned through foundation parameters. This finding is valuable in optimizing structural elements under dynamic loading, especially for applications involving curved concrete components in smart infrastructure.

Fig. 11 investigates the influence of shell geometry—specifically the arc length to total length ratio—on RFC as a function of K_P^*. A clear pattern emerges, where higher S/L ratios result in lower RFC values at equivalent K_P^*. This suggests that increasing the arc length of the cylindrical shell reduces its natural frequency sensitivity to foundation stiffness. Notably, at higher K_P^* values, the impact of the shell's geometry becomes more significant. The results imply that shells with greater curvature (larger arc lengths) distribute stresses more evenly and are less susceptible to foundation-induced vibrational amplification. This insight is critical in the design of curved concrete panels reinforced by nano-alumina, providing a guideline to tailor structural curvature for vibration control. The graph further supports the potential for geometric tuning to mitigate vibrational response in nano-composite-enhanced shell structures.

Fig. 12 illustrates the relationship between the radius-to-length ratio and RFC for varying arc length-to-length ratios. The curves indicate a mild downward trend in RFC as R/L increases, leveling off at higher values. The results reveal that increasing the radius—resulting in a flatter shell—slightly reduces the relative frequency response, particularly for smaller S/L values. The effect, however, is marginal across the studied range, suggesting that radius plays a less dominant role in vibrational characteristics compared to other geometric parameters. Nonetheless, this observation is important in the context of large-span structures where radius may significantly influence construction feasibility. The small changes in RFC highlight the structural stability of nano-alumina-reinforced shells across a wide range of curvature configurations, affirming their robustness in practical deployment scenarios.

Fig. 13 evaluates how variations in K_W^*, the Winkler foundation stiffness parameter, influence the RFC as a function of the radius-to-length ratio. The curves show a prominent reduction in RFC with increasing R/L, stabilizing after a certain point. Higher K_W^* values notably increase the RFC across the entire R/L range, with the most dramatic effects occurring at low R/L values (i.e., more curved shells). This indicates that highly curved panels are more sensitive to subgrade stiffness, and thus the vibrational response can be strongly influenced by the foundation behavior. As the shell becomes flatter (higher R/L), the impact of K_W^* diminishes. These results are vital for engineering applications requiring dynamic stability on elastic foundations, and they highlight the effectiveness of nano-alumina reinforcement in maintaining performance across different curvature levels.

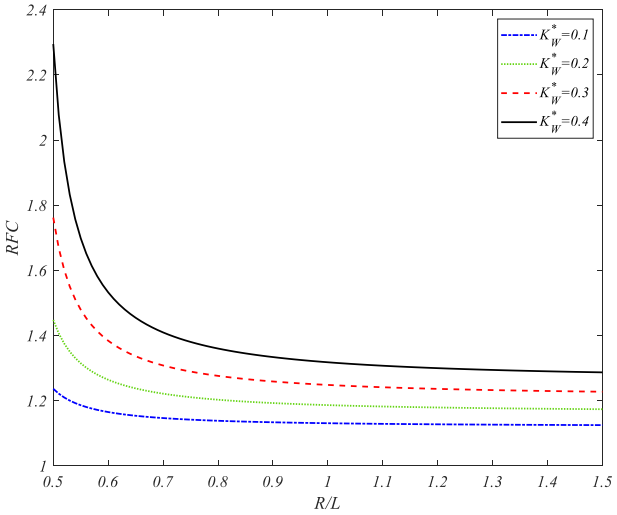

Fig. 13 The relationship between the radius-to-length ratio and RFC for varying K_W^* values

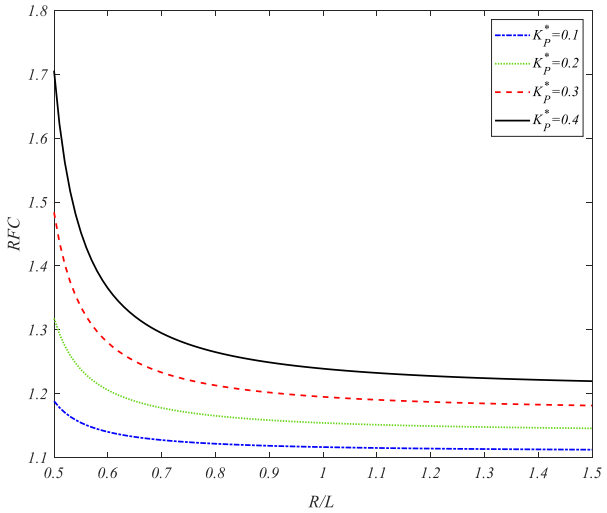

Fig. 14 The effect of varying the dimensionless Pasternak foundation parameter on the relative frequency change with respect to the radius-to-length ratio

Fig. 14 explores the effect of varying the dimensionless Pasternak foundation parameter on the relative frequency change with respect to the radius-to-length ratio. The plots reveal a steep decline in RFC as R/L increases from 0.5 to around 1.0, after which the trend stabilizes. Higher K_P^* values consistently result in elevated RFC levels across the R/L range, highlighting the enhanced stiffness and frequency response due to increased shear layer interaction in the Pasternak foundation model. This sensitivity is especially prominent at low R/L, where shell curvature is more pronounced, indicating stronger foundation-structure interaction. As the shell becomes flatter (higher R/L), the influence of the subgrade shear parameter diminishes, yielding more uniform frequency behavior. These results underscore the importance of curvature in tuning dynamic performance, and confirm that Pasternak-type foundations are highly effective for controlling vibrations in nano-alumina-reinforced cylindrical concrete panels.

5. Conclusions

This study comprehensively investigated the vibrational response of curved concrete shell panels reinforced with nano-alumina particles, focusing on the influence of geometric parameters, nanoparticle distribution, and elastic foundation stiffness. By incorporating nano-alumina into the concrete matrix, the structural performance of the panels under dynamic loading conditions was significantly enhanced. The analysis demonstrated that the addition of nano-alumina effectively increased the natural frequencies of the panels, particularly when the reinforcement was non-uniformly distributed in optimized patterns. This improvement was attributed to the superior mechanical characteristics of nano-alumina, including its high stiffness and strength at the nanoscale, which contributed to improved load transfer and energy dissipation within the structure. The study further examined the impact of geometric configurations, including the radius-to-length and thickness-to-length ratios, revealing that thinner and more curved panels exhibited higher sensitivity to changes in reinforcement and foundation stiffness. The incorporation of Winkler and Pasternak elastic foundations provided a realistic simulation of support conditions, and the results showed that both parameters significantly influenced the vibrational characteristics. Higher foundation stiffnesses led to increased natural frequencies, underscoring the importance of boundary conditions in dynamic behavior. To assess the relative change in vibrational behavior due to these parameters, the concept of Relative Frequency change was introduced and employed effectively. Finally, the present formulation was validated against results obtained using Classical Plate Theory and Reddy's third-order shear deformation theory. The comparisons confirmed the accuracy and efficiency of the proposed approach, particularly in capturing the effects of nanoscale reinforcement. Overall, the findings of this research provided valuable insights into the design of nano-reinforced shell structures and highlighted the potential of nanotechnology in enhancing the dynamic performance of concrete infrastructure. These results offered practical implications for the development of high-performance, vibration-resistant structural systems.

Acknowledgement

The authors extend their appreciation to the Deanship of Scientific Research at King Khalid University for funding this work through Large Groups [grant number RGP.2/ 419/46].

Funding

This work was supported by Supported by the scientific research and innovation team construction project of Luzhou vocational and Technical College (2021YJTD07) and Luzhou Science and Technology Program (2024JYJ95091).

References

Akbari, H., Azadi, M. and Fahham, H. (2022), "Free vibration analysis of thick sandwich cylindrical panels with saturated fg-porous core", *Mech. Based Des. Struct.*, **50**(4), 1268-1286. https://doi.org/10.1080/15397734.2020.1748051.

Al-Houri, S., Al-Osta, M.A., Gawah, Q., Bourada, F., Tounsi, A., Al-Dulaijan, S.U. and Tounsi, A. (2024), "Wave propagation analysis of composite beams reinforced with nonlinear fg-cnt distributions supported on kerr elastic foundation utilizing an improved integral first-order shear deformation theory", *Geomech. Eng.*, **39**(5), 483. https://doi.org/10.12989/gae.2024.39.5.483.

Arani, A.G., Kiani, F. and Afshari, H. (2021), "Free and forced vibration analysis of laminated functionally graded CNT-reinforced composite cylindrical panels", *J. Sandw. Struct. Mater.*, **23**(1), 255-278. https://doi.org/10.1177/1099636219830787.

Azmi, M., Kolahchi, R. and Bidgoli, M.R. (2019), "Dynamic analysis of concrete column reinforced with sio2 nanoparticles subjected to blast load", *Adv. Concr. Constr.*, **7**(1), 51. https://doi.org/10.12989/acc.2019.7.1.051.

Beitollahi, A., Janghorban, M., Bazargan-Lari, Y. and Tounsi, A. (2025), "On the variable length scale parameter for agglomeration of nanoparticles in nanocomposites", *Proceedings of the Institution of Mechanical Engineers, Part C: Journal of Mechanical Engineering Science*, 09544062241308513. https://doi.org/10.1177/09544062241308513.

Belabed, Z., Bousahla, A.A. and Tounsi, A. (2024a), "Vibrational and elastic stability responses of functionally graded carbon nanotube reinforced nanocomposite beams via a new quasi-3d finite element model", *Comput. Concr.*, **34**(5), 625-648. https://doi.org/10.12989/cac.2024.34.5.625.

Belabed, Z., Tounsi, A., Bousahla, A.A., Tounsi, A., Khedher, K.M. and Salem, M.A. (2024b), "Mechanical behavior analysis of fg-cntrc porous beams resting on winkler and pasternak elastic foundations: a finite element approach", *Comput. Concr.*, **34**(4), 447-476. https://doi.org/10.12989/cac.2024.34.4.447.

Bentrar, H., Chorfi, S.M., Belalia, S.A., Tounsi, A., Ghazwani, M.H. and Alnujaie, A. (2023), "Effect of porosity distribution on free vibration of functionally graded sandwich plate using the p-version of the finite element method", *Struct. Eng. Mech.*, **88**(6), 551-567. https://doi.org/10.12989/sem.2023.88.6.551.

Buaria, D. and Sreenivasan, K.R. (2023), "Forecasting small-scale dynamics of fluid turbulence using deep neural networks", *Proceedings of the National Academy of Sciences*, **120**(30), e2305765120. https://doi.org/10.1073/pnas.2305765120.

Chen, C., Yang, H., Song, K., Liang, D., Zhang, Y. and Ni, J. (2023), "Dissolution feature differences of carbonate rock within hydro-fluctuation belt located in the three gorges reservoir area", *Eng. Geol.*, **327**, 107362. https://doi.org/10.1016/j.enggeo.2023.107362.

Ebrahimi, F., Dehghan, M. and Seyfi, A. (2019a), "Eringen's nonlocal elasticity theory for wave propagation analysis of magneto-electro-elastic nanotubes", *Adv. Nano Res.*, **7**(1), 1. https://doi.org/10.12989/anr.2019.7.1.001.

Ebrahimi, F., Dehghan, M. and Seyfi, A. (2019b), "Eringen's nonlocal elasticity theory for wave propagation analysis of magneto-electro-elastic nanotubes", *Adv. Nano Res.*, **7**(1), 1. https://doi.org/10.12989/anr.2019.7.1.001.

Eshaghi, M.S., Anitescu, C., Thombre, M., Wang, Y., Zhuang, X. and Rabczuk, T. (2025), "Variational physics-informed neural operator (vino) for solving partial differential equations", *Comput. Meth. Appl. Mech. Eng.*, **437**, 117785. https://doi.org/10.1016/j.cma.2025.117785.

Feng, Y., Mohammadi, M., Wang, L., Rashidi, M. and Mehrabi, P. (2021), "Application of artificial intelligence to evaluate the fresh properties of self-consolidating concrete", *Materials*, **14**(17), 4885. https://doi.org/10.3390/ma14174885.

Firouzianhaji, A., Usefi, N., Samali, B. and Mehrabi, P. (2021), "Shake table testing of standard cold-formed steel storage rack", *Appl. Sci.*, **11**(4), 1821. https://doi.org/10.3390/app11041821.

Fu, L., Huang, A., Gu, H. and Ni, H. (2018), "Properties and microstructures of lightweight alumina containing different types of nano-alumina", *Ceram. Int.*, **44**(15), 17885-17894. https://doi.org/10.1016/j.ceramint.2018.06.261.

Gawah, Q., Bourada, F., Al-Osta, M.A., Tahir, S.I., Tounsi, A. and Yaylacı, M. (2024), "An improved first-order shear deformation theory for wave propagation analysis in fg-cntrc beams resting on a viscoelastic substrate", *Int. J. Struct. Stabil. Dyn.*, **25**(1), 2550010. https://doi.org/10.1142/S0219455425500105.

Gawah, Q., Al-Osta, M.A., Bourada, F., Tounsi, A., Ahmad, S. and Al-Zahrani, M.M. (2025), "Bending analysis of graphene platelet-reinforced fg plates on kerr foundations using an integral hsdt", *Acta Mechanica*. 1-25. https://doi.org/10.1007/s00707-025-04236-6.

Goswami, S., Anitescu, C., Chakraborty, S. and Rabczuk, T. (2020), "Transfer learning enhanced physics informed neural network for phase-field modeling of fracture", *Theor. Appl. Fract. Mech.*, **106**, 102447. https://doi.org/10.1016/j.tafmec.2019.102447.

Guo, H., Zhuang, X. and Rabczuk, T. (2021), "A deep collocation method for the bending analysis of kirchhoff plate", *arXiv preprint arXiv:2102.02617*. https://doi.org/10.32604/cmc.2019.06660.

Hajmohammad, M.H., Zarei, M.S., Farrokhian, A. and Kolahchi, R. (2018), "A layerwise theory for buckling analysis of truncated conical shells reinforced by cnts and carbon fibers integrated with piezoelectric layers in hygrothermal environment", *Adv. Nano Res.*, **6**(4), 299. https://doi.org/10.12989/anr.2018.6.4.299.

Han, S., Zheng, D., Mehdizadeh, B., Nasr, E.A., Khandaker, M.U., Salman, M. and Mehrabi, P. (2023a), "Sustainable design of self-consolidating green concrete with partial replacements for cement through neural-network and fuzzy technique", *Sustainability*, **15**(6), 4752. https://doi.org/10.3390/su15064752.

Han, S., Zhu, Z., Mortazavi, M., El-Sherbeeny, A.M. and Mehrabi, P. (2023b), "Analytical assessment of the structural behavior of a specific composite floor system at elevated temperatures using a newly developed hybrid intelligence method", *Buildings*, **13**(3), 799. https://doi.org/10.3390/buildings13030799.

He, L., Guo, H., Jin, Y., Zhuang, X., Rabczuk, T. and Li, Y. (2022), "Machine-learning-driven on-demand design of phononic beams", *Sci. China Phys. Mech. Astr.*, **65**(1), 214612. https://doi.org/10.1007/s11433-021-1787-x.

Hu, D., Sun, H., Mehrabi, P., Ali, Y.A. and Al-Razgan, M. (2023), "Application of artificial intelligence technique in optimization and prediction of the stability of the walls against wind loads in building design", *Mech. Adv. Mater. Struct.*, 1-18. https://doi.org/10.1080/15376494.2023.2206208.

Huang, H., Li, M., Yuan, Y. and Bai, H. (2022), "Theoretical analysis on the lateral drift of precast concrete frame with replaceable artificial controllable plastic hinges", *J. Build. Eng.*, **62**, 105386. https://doi.org/10.1016/j.jobe.2022.105386.

Jayakumari, B.Y., Swaminathan, E.N. and Partheeban, P. (2024), "Sustainable construction material using nanosilica and multi-walled carbon nanotubes in cement concrete", *Adv. Nano Res.*, **16**(5), 459-472. https://doi.org/10.12989/.2024.16.5.459.

Khdeir, A., Reddy, J. and Frederick, D. (1989), "A study of bending, vibration and buckling of cross-ply circular cylindrical shells with various shell theories", *Int. J. Eng. Sci.*, **27**(11), 1337-1351. https://doi.org/10.1016/0020-7225(89)90058-X.

Khorshidi, H., Zhang, C., Najafi, E. and Ghasemi, M. (2022), "Fresh, mechanical and microstructural properties of alkali-

activated composites incorporating nanomaterials: A comprehensive review", *J. Clean. Prod*., 135390. https://doi.org/10.1016/j.jclepro.2022.135390.

Lamond, J.F. and Pielert, J.H. (2006), *Significance of Tests and Properties of Concrete and Concrete-Making Materials*, ASTM International, **169**. https://doi.org/10.1520/STP169D-EB.

Li, D., Chen, Q., Wang, H., Shen, P., Li, Z. and He, W. (2024), "Deep learning-based acoustic emission data clustering for crack evaluation of welded joints in field bridges", *Automat. Constr*., **165**, 105540. https://doi.org/https://doi.org/10.1016/j.autcon.2024.105540

Li, Z., Li, H. and Meng, L. (2023), "Model compression for deep neural networks: A survey", *Computers*, **12**(3), 60. https://doi.org/10.3390/computers12030060.

Liu, J., Mohammadi, M., Zhan, Y., Zheng, P., Rashidi, M. and Mehrabi, P. (2021a), "Utilizing artificial intelligence to predict the superplasticizer demand of self-consolidating concrete incorporating pumice, slag, and fly ash powders", *Materials*, **14**(22), 6792. https://doi.org/10.3390/ma14226792.

Liu, T., Wang, A., Wang, Q., Qin, B. and Xie, F. (2021b), "Chebyshev formulation for in-plane vibration analysis of arbitrary laminated polygonal plates", *AIAA J*., **59**(7), 2753-2767. https://doi.org/10.2514/1.J060366.

Liu, X., Liu, X., Zhang, Z. and Ai, X. (2024), "Effect of carbonation curing on the characterization and properties of steel slag-based cementitious materials", *Cement Concr. Compos*., **154**, 105769. https://doi.org/10.1016/j.cemconcomp.2024.105769.

Long, X., Iyela, P.M., Su, Y., Atlaw, M.M. and Kang, S.B. (2024), "Numerical predictions of progressive collapse in reinforced concrete beam-column sub-assemblages: A focus on 3d multiscale modeling", *Eng. Struct*., **315**, 118485. https://doi.org/10.1016/j.engstruct.2024.118485.

Madenci, E., Ozkilic, Y.O., Hakamy, A. and Tounsi, A. (2023), "Experimental tensile test and micro-mechanic investigation on carbon nanotube reinforced carbon fiber composite beams", *Adv. Nano Res*., **14**(5), 443-450. https://doi.org/10.12989/anr.2023.14.5.443.

Mehrabi, P., Shariati, M., Kabirifar, K., Jarrah, M., Rasekh, H., Trung, N.T., Shariati, A. and Jahandari, S. (2021a), "Effect of pumice powder and nano-clay on the strength and permeability of fiber-reinforced pervious concrete incorporating recycled concrete aggregate", *Constr. Build. Mater*., **287**, 122652. https://doi.org/10.1016/j.conbuildmat.2021.122652.

Mehrabi, P., Honarbari, S., Rafiei, S., Jahandari, S. and Alizadeh Bidgoli, M. (2021b), "Seismic response prediction of frc rectangular columns using intelligent fuzzy-based hybrid metaheuristic techniques", *J. Ambient Intell. Human. Comput*., **12**, 10105-10123. https://doi.org/10.1007/s12652-020-02776-4.

Mehrabi, P., Dackermann, U., Siddique, R. and Rashidi, M. (2024), "A review on the effect of synthetic fibres, including macro fibres, on the thermal behaviour of fibre-reinforced concrete", *Buildings*, **14**(12), 4006. https://doi.org/10.3390/buildings14124006.

Mehrabi, P., Mortazavi, M. and Far, H. (2025), "Axisymmetric thermal post-buckling of the eccentric annular sector plate made of gori-metamaterials: introducing dnn-rf algorithm for solving the post-buckling problems", *Thin Wall. Struct*., **208**, 112795. https://doi.org/10.1016/j.tws.2024.112795.

Moradi, H., Atashi, P., Amelirad, O., Yang, J.K., Chang, Y.Y. and Kamranifard, T. (2022), "Machine learning modeling and doe-assisted optimization in synthesis of nanosilica particles via stöber method", *Adv. Nano Res*., **12**(4), 387. https://doi.org/10.12989/anr.2022.12.4.387.

Mortazavi, B., Zhuang, X., Rabczuk, T. and Shapeev, A.V. (2023), "Atomistic modeling of the mechanical properties: The rise of machine learning interatomic potentials", *Mater. Horizons*, **10**(6), 1956-1968. https://doi.org/10.1039/D3MH00125C.

Niu, Y., Wang, W., Su, Y., Jia, F. and Long, X. (2024), "Plastic damage prediction of concrete under compression based on deep learning", *Acta Mechanica*. **235**(1), 255-266. https://doi.org/10.1007/s00707-023-03743-8.

Reddy, J. and Liu, C. (1985), "A higher-order shear deformation theory of laminated elastic shells", *Int. J. Eng. Sci*., **23**(3), 319-330. https://doi.org/10.1016/0020-7225(85)90051-5.

Rong, C., Peng, Y., Shi, Q. and Wang, P. (2025), "Eccentric compression performance of concrete filled steel tube slotted columns: Experiment and simulation analysis", *Structures*, **74**, 108580. https://doi.org/10.1016/j.istruc.2025.108580.

Samaniego, E., Anitescu, C., Goswami, S., Nguyen-Thanh, V. M., Guo, H., Hamdia, K., Zhuang, X. and Rabczuk, T. (2020), "An energy approach to the solution of partial differential equations in computational mechanics via machine learning: Concepts, implementation and applications", *Comput. Meth. Appl. Mech. Eng*., **362**, 112790. https://doi.org/10.1016/j.cma.2019.112790.

Song, K., Yang, H., Liang, D., Chen, L. and Jaboyedoff, M. (2024), "Step-like displacement prediction and failure mechanism analysis of slow-moving reservoir landslide", *J. Hydrol*., **628**, 130588. https://doi.org/10.1016/j.jhydrol.2023.130588.

Sun, G., Kong, G., Liu, H. and Amenuvor, A.C. (2017), "Vibration velocity of x-section cast-in-place concrete (xcc) pile-raft foundation model for a ballastless track", *Canadian Geotech. J*., **54**(9), 1340-1345. https://doi.org/10.1139/cgj-2015-0623.

Taheri, E., Firouzianhaji, A., Usefi, N., Mehrabi, P., Ronagh, H. and Samali, B. (2019), "Investigation of a method for strengthening perforated cold-formed steel profiles under compression loads", *Appl. Sci*., **9**(23), 5085. https://doi.org/10.3390/app9235085.

Taheri, E., Firouzianhaji, A., Mehrabi, P., Vosough Hosseini, B. and Samali, B. (2020), "Experimental and numerical investigation of a method for strengthening cold-formed steel profiles in bending", *Appl. Sci*., **10**(11), 3855. https://doi.org/10.3390/app10113855.

Taheri, E., Mehrabi, P., Rafiei, S. and Samali, B. (2021), "Numerical evaluation of the upright columns with partial reinforcement along with the utilisation of neural networks with combining feature-selection method to predict the load and displacement", *Appl. Sci*., **11**(22), 11056. https://doi.org/10.3390/app112211056.

Toghroli, A., Mehrabi, P., Shariati, M., Trung, N.T., Jahandari, S. and Rasekh, H. (2020), "Evaluating the use of recycled concrete aggregate and pozzolanic additives in fiber-reinforced pervious concrete with industrial and recycled fibers", *Constr. Build. Mater*., **252**, 118997. https://doi.org/10.1016/j.conbuildmat.2020.118997.

Tounsi, A., Belabed, Z., Bounouara, F., Balubaid, M., Mahmoud, S., Bousahla, A.A. and Tounsi, A. (2024), "A finite element approach for forced dynamical responses of porous FG nanocomposite beams resting on viscoelastic foundations", *Int. J. Struct. Stabil. Dyn*., 2650078. https://doi.org/10.1142/S0219455426500781.

Wang, X., Li, L., Wei, M., Xiang, Y., Wu, Y., Zhou, B., Sun, Y. and Cheng, W. (2025), "Experimental study on the mechanical properties of short-cut basalt fiber reinforced concrete under large eccentric compression", *Sci. Rep*., **15**(1), 10845. https://doi.org/10.1038/s41598-025-94964-5.

Wu, J., Yang, Y., Mehrabi, P. and Nasr, E.A. (2023), "Efficient machine-learning algorithm applied to predict the transient shock reaction of the elastic structure partially rested on the viscoelastic substrate", *Mech. Adv. Mater. Struct*., 1-25. https://doi.org/10.1080/15376494.2023.2183289.

Wu, Y., Li, Y., Yuan, H., Zhang, R., Jiang, Y., Liang, C., Zhu, Z.,

Liang, C. and Wang, X. (2024), "Efficient multi-objective coil design with deep neural network-accelerated pso in wpt systems", *Proceedings of the 2024 IEEE Transportation Electrification Conference and Expo, Asia-Pacific (ITEC Asia-Pacific), IEEE*, 956-961. https://doi.org/10.1109/ITECAsia-Pacific63159.2024.10738618.

Xia, L., Wang, R., Chen, G., Asemi, K. and Tounsi, A. (2023), "The finite element method for dynamics of fg porous truncated conical panels reinforced with graphene platelets based on the 3-d elasticity", *Adv. Nano Res.*, **14**(4), 375-389. https://doi.org/10.12989/.2023.14.4.375.

Yang, H., Chen, C., Ni, J. and Karekal, S. (2023a), "A hyper-spectral evaluation approach for quantifying salt-induced weathering of sandstone", *Sci. Total Environ.*, **885**, 163886. https://doi.org/10.1016/j.scitotenv.2023.163886.

Yang, H., Song, K., Chen, L. and Qu, L. (2023b), "Hysteresis effect and seasonal step-like creep deformation of the jiuxianping landslide in the three gorges reservoir region", *Eng. Geol.*, **317**, 107089. https://doi.org/10.1016/j.enggeo.2023.107089.

Yang, H., Qu, L., Chen, L., Song, K., Yang, Y. and Liang, Z. (2024a), "Potential sliding zone recognition method for the slow-moving landslide based on the hurst exponent", *J. Rock Mech. Geotech. Eng.*, **16**(10), 4105-4124. https://doi.org/10.1016/j.jrmge.2023.08.007.

Yang, H., Huang, G., Chen, C., Yang, Y., Wang, Q. and Dai, X. (2024b), "Method for evaluation of geological strength index of carbonate cliff rocks: Coupled hyperspectral-digital borehole image technique", *J. Rock Mech. Geotech. Eng.*, **16**(10), 4204-4215. https://doi.org/10.1016/j.jrmge.2024.08.013.

Ye, W., Shi, Y., Zhou, Q., Xie, M., Wang, H., Bou-Saïd, B. and Liu, W. (2024), "Recent advances in self-lubricating metal matrix nanocomposites reinforced by carbonous materials: A review", *Nano Mater. Sci.*, **6**(6), 701-713. https://doi.org/10.1016/j.nanoms.2024.02.007.

Youzera, H., Meftah, S.A., Tounsi, A., Salem, M.A., Khedher, K.M. and Yaylacı, M. (2025), "Free vibration analysis of sandwich cylindrical shells with functionally graded carbon nanotube-reinforced composite face sheets using the differential quadrature (dq) method", *Acta Mechanica*, 1-16. https://doi.org/10.1007/s00707-025-04230-y.

Zerrouki, R., Karas, A. and Zidour, M. (2020), "Critical buckling analyses of nonlinear fg-cnt reinforced nano-composite beam", *Adv. Nano Res.*, **9**(3), 211-220. https://doi.org/10.12989/anr.2020.9.3.211.

Zhang, W., Liu, X., Huang, Y. and Tong, M.N. (2022), "Reliability-based analysis of the flexural strength of concrete beams reinforced with hybrid bfrp and steel rebars", *Arch. Civil Mech. Eng.*, **22**(4), 171. https://doi.org/10.1007/s43452-022-00493-7.

Zhang, W., Yang, X., Lin, J., Lin, B. and Huang, Y. (2024), "Experimental and numerical study on the torsional behavior of rectangular hollow reinforced concrete columns strengthened by CFRP", *Structures*, **70**, 107690. https://doi.org/10.1016/j.istruc.2024.107690.

Zhang, Z., Guo, F., Gao, J., Deng, E., Kong, J. and Zhang, L. (2025), "Seismic performance of an innovative prefabricated bridge pier using rapid hardening ultra-high performance concrete", *Structures*, **74**, 108558. https://doi.org/10.1016/j.istruc.2025.108558.

Zhao, T., Chen, Y., Ma, X., Linghu, S. and Zhang, G. (2022), "Free transverse vibration analysis of general polygonal plate with elastically restrained inclined edges", *J. Sound Vib.*, **536**, 117151. https://doi.org/10.1016/j.jsv.2022.117151.

Zhuang, X., Guo, H., Alajlan, N., Zhu, H. and Rabczuk, T. (2021), "Deep autoencoder based energy method for the bending, vibration, and buckling analysis of kirchhoff plates with transfer learning", *Eur. J. Mech. A Solids*, **87**, 104225. https://doi.org/10.1016/j.euromechsol.2021.104225.

CC